Charge density wave order, local lattice distortions, and topological electronic states in NbTe$_4$

V. Petkov[1,*] R. Amin,[1] M. Jakhar,[1] V. Barone,[1] AM Milinda Abeykoon,[2] M. Sretenovic,[3] and X. Ke[3]

[1]*Department of Physics, Central Michigan University, Mt. Pleasant, Michigan 48858, USA*
[2]*Photon Sciences Division, Brookhaven National Laboratory, Upton, New York 11973, USA*
[3]*Department of Physics and Astronomy, Michigan State University, East Lansing, Michigan 48824, USA*

Assessing the atomic and electronic structure of strongly correlated systems in which the crystal symmetry changes due to emergent lattice distortions, such as charge density waves (CDWs), is nontrivial because the distortions are not necessarily amenable to a traditional crystallographic description. Using advance scattering and modeling techniques, we reveal the evolution of the atomic displacement modes behind the CDW phases of quasi-one-dimensional NbTe$_4$ and derive the so far unknown atomic structure of its low-temperature commensurate (C) CDW phase. Electronic structure calculations based on the experimental C-CDW structure data predict the existence of Dirac fermions whose multiplicity turns out to depend on the degree of lattice distortions accounted for in the experimental structure derivation. We argue that the electronic structure of CDW systems in general, and in particular in transition metal tetratellurides, can be strongly impacted by local lattice distortions and, therefore, they should be fully accounted for when their rich physics is considered.

I. INTRODUCTION

Low-dimensional transition metal (TM) chalcogenides exhibit a rich diagram of charge density wave (CDW) phases and unusual physical properties resulting from the presence of strong correlations between spin, electronic, and lattice degrees of freedom, including metal-insulator transitions, superconductivity (SC), and topological states [1–8]. To understand the properties, a good knowledge of the crystal structure is needed. The knowledge, however, is nontrivial to obtain because lattice distortions accompanying the formation of CDWs are not necessarily amenable to a traditional crystallographic description. A typical example is quasi-one-dimensional NbTe$_4$. Similar to its sister compound TaTe$_4$, it exhibits lattice distortions due to the emergence of CDW order and becomes a superconductor under high pressure [9,10]. Unlike TaTe$_4$, however, the lattice distortions in NbTe$_4$ undergo a complex temperature evolution resulting in a series of phase transitions between three distinct CDW phases. Furthermore, its ground state CDW structure is not well known. This makes it difficult to assess the interplay between the SC and CDW orders in NbTe$_4$ and explore its electronic structure for fermionic excitations [6–8].

In particular, at high temperature, both NbT$_4$ and TaTe$_4$ adopt a tetragonal structure with a ten-atom unit cell and space group (S.G.) *P4/mcc* symmetry [11–15]. In the structure, chains of uniformly spaced TM atoms run in parallel to the *c* axis of the crystal lattice, passing through rectangles of Te atoms coupled by Te-Te dimerlike bonds, as shown in Fig. 1. With decreasing temperature below 475 K for TaTe$_4$ and 520 K for NbTe$_4$, lattice distortions involving both TM and Te atoms develop due to the emergence of CDW order. The distortions include a correlated displacement of TM atoms along the chains to form trimers, leading to doubling of the *a* axis and tripling of the *c* axis of the tetragonal unit cell of the undistorted lattice. In NbTe$_4$, there are three types of Nb chains where two of them have incommensurate distortions and the third chain suffers a very weak distortion. Hence, at room temperature, NbTe$_4$ exhibits an incommensurate (IC$_1$)-CDW order. The lattice distortions in TaTe$_4$ are as above but are commensurate with the crystal lattice. Thus, TM tetratellurides appear to be the only reported strongly correlated systems in which three distinct lattice distortion modes related to emergent CDW order coexist.

The structure of the C-CDW phase of TaTe$_4$ has been determined by single-crystal experiments and described in terms of a 120-atom, $2a \times 2a \times 3c$ supercell with tetragonal S.G. *P4/ncc* symmetry [16]. Based on the experimental crystal structure data, the electronic band structure has been computed and the emergence of fermionic excitations, including double Dirac fermions, predicted [6]. For NbTe$_4$, the IC$_1$-CDW structure has been determined at room temperature by single-crystal experiments using a superspace formalism [17]. It has been found that it evolves with decreasing temperature and transforms to a distinct IC$_2$-CDW structure via a rare incommensurate-to-incommensurate CDW phase transition [12,18,19,20]. The IC$_2$-CDW structure has also been determined using a superspace formalism. In addition, a commensurate approximation to it based on a 120-atom, $2a \times 2a \times 3c$ supercell with tetragonal S.G. *P4* symmetry has been derived [21]. Upon further cooling, C-CDW order emerges at 50 K. The C-CDW structure of NbTe$_4$ is assumed to share common structural features with that of room-temperature C-CDW TaTe$_4$, but this assumption has not been rigorously proven. The question as to what drives the evolution of IC-
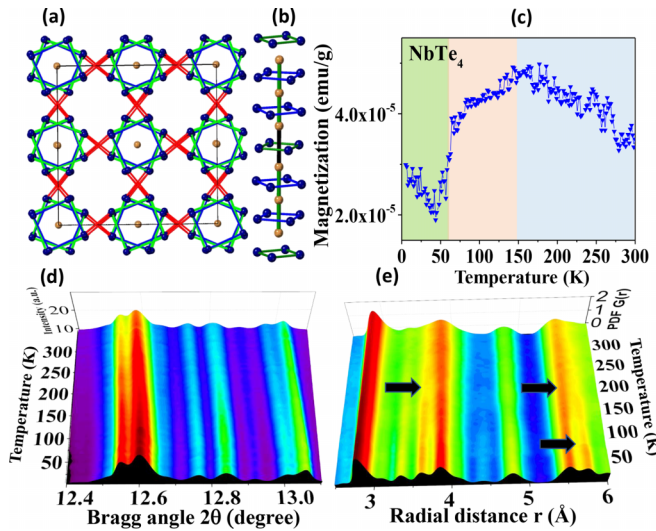
*petko1vg@cmich.edu

174112-1

FIG. 1. (a) Projection of the crystal structure of $NbTe_4$ down the c axis of a $2a \times 2a \times 3c$ tetragonal lattice (outlined). It features (b) strings of Nb atoms (brown circles) passing through rectangles of Te atoms (dark-blue circles). (c) Temperature dependence of the magnetization for $NbTe_4$. Areas shaded in different colors highlight temperature ranges where it shows distinct variation with temperature and the material exhibits IC_1-CDW (blue), IC_2-CDW (light red), and C-CDW (green) order. Color map of selected Bragg peaks in the XRD pattern (d) and low-r peaks in the PDFs (e) for $NbTe_4$ as a function of temperature. Arrows mark changes in PDF features, i.e., atomic-pair distances, accompanying the IC_1-CDW to IC_2-CDW and IC_2-CDW to C-CDW phase transitions.

CDW order in $NbTe_4$ into C-CDW order with decreasing temperature has also remained unclear. Using atomic-pair distribution function (PDF) analysis and computer modeling, we reveal the evolution of the $NbTe_4$ structure over a broad temperature range, including the IC_1-CDW to IC_2-CDW and IC_2-CDW to C-CDW phase transitions. The advantage of this approach is that it takes into account both the sharp and the diffuse features of the diffraction data allowing us to simultaneously explore and refine both the longer range and the local structural features of CDW phases. The resulting structure models provide a sound basis for electronic structure calculations, allowing us to explore high-symmetry features of the Brillouin zone of C-CDW $NbTe_4$.

II. EXPERIMENT

High-quality $NbTe_4$ crystal was synthesized following the growth conditions described in [9]. To assess the interplay between the electronic properties and emergent CDW order, we measured the magnetization using a physical property measurement system from Quantum Design. As can be seen in Fig. 1(c), the magnetization exhibits inflection points at about 150 K and 50 K, which, similar to the inflection points exhibited by the electrical resistivity [10,22,23], can be associated with the IC_1-CDW to IC_2-CDW and IC_2-CDW to C-CDW phase transitions, respectively. The result shows that the CDW order in $NbTe_4$ affects its electronic properties significantly.

Synchrotron x-ray diffraction (XRD) experiments were conducted at the beamline 28-ID-1 at the National

Synchrotron Light Source-II, Brookhaven National Laboratory using x rays with energy of 74.46 keV ($\lambda = 0.1665$ Å). The sample was sealed in a Kapton tube and positioned inside a liquid He cryostat used to control its temperature. XRD data were taken in the range from 10 K to 300 K in transmission geometry. Scattered intensities were collected using a PerkinElmer area detector positioned 204 mm away from the sample to reach wave vectors q_{max} as high as 28 Å^{-1}, which is necessary to obtain high real-space resolution atomic PDFs. The PDFs were derived from the XRD patterns using standard procedures [24]. XRD and PDF intensity color maps are shown in Figs. 1(d) and 1(e). Because the XRD data include both principal Bragg peaks and superstructure satellites (see Fig. S1 in the Supplemental Material [25]), the experimental PDF data directly show the evolution of both the average crystal lattice and its distortions with temperature, including changes in atomic-pair distances taking place in the vicinity of IC_1-CDW to IC_2-CDW and IC_2-CDW to C-CDW phase transitions [see arrows in Fig. 1(e)].

III. CRYSTAL STRUCTURE MODELING

A. Assessing lattice distortions in $NbTe_4$ by small-size structure modeling

To investigate changes in the average crystal lattice in $NbTe_4$ in the temperature range from 50 K to 300 K, we performed Rietveld analysis of the respective XRD data sets employing the S.G. $P4$ model, which was found useful in approximating its IC_2-CDW phase. To investigate changes in the temperature range from 10 K to 50 K, we performed a Rietveld analysis of the respective XRD data sets using the S.G. $P4/ncc$ model, which was found useful in describing the structure of C-CDW $TaTe_4$. The models share a common tetragonal $2a \times 2a \times 3c$ supercell but have a different number of refinable parameters. The computations were done with the help of the software FULLPROF [26]. Both models fit the XRD patterns very well, as demonstrated in Figs. 2(a) and 2(b). Indeed, the Rietveld results changed little when either the S.G. $P4$ or the S.G. $P4/ncc$ model was used to fit the XRD patterns for the whole 10–300 K temperature range. For completeness, Rietveld refined supercell parameters for both models are shown in Fig. 3 (left). As can be seen in the figure, values for the supercell parameters $a_S (a_S = 2a)$ and $c_S (c_S = 3c)$ gradually decrease with decreasing temperature down to about 50 K where the rate of their decrease diminishes sharply, reflecting the IC_2-CDW to C-CDW phase transition. Changes in that rate in the vicinity of the IC_1-CDW to IC_2-CDW transition (150 K) are subtle, reflecting its sluggish nature [20,27,28].

Next, we used the Rietveld refined structure models as an input to fits to the respective atomic PDFs, which are known to have an increased sensitivity to local lattice distortions [29–35]. Structure models derived from Rietveld refinements alone captured the basic PDF features but failed in many important details, as shown in Figs. 2(c) and 2(d). Once the models are refined further against the PDF data, the agreement is improved, as shown in Figs. 2(e) and 2(f). Here, again, the values for the PDF-refined supercell parameters and their temperature dependence changed little when either the S.G. $P4$ or the S.G. $P4/ncc$ superstructure model was used to fit the PDF patterns for the whole 10–300 K temperature range.
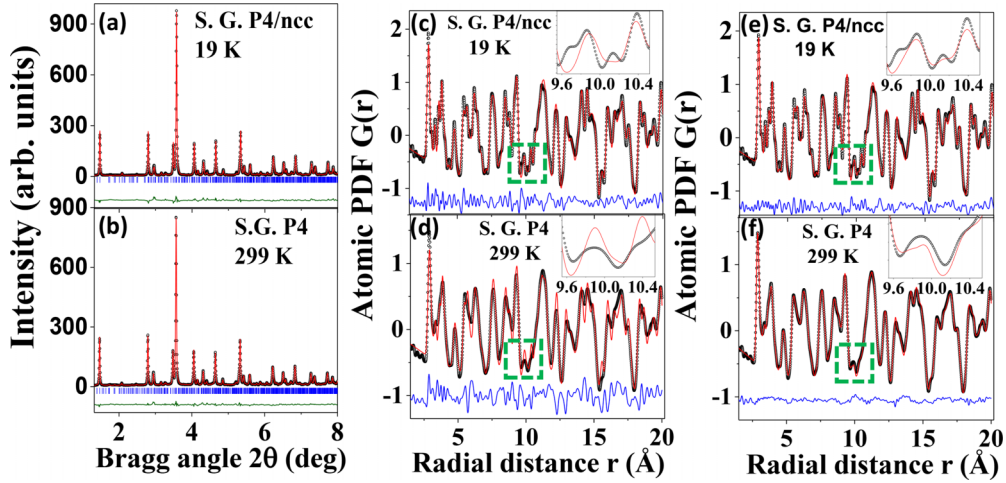
FIG. 2. (a), (b) Rietveld fits (red line) to XRD patterns (black symbols) for NbTe$_4$ obtained at 299 K and 19 K where the material exhibits IC$_1$-CDW and C-CDW order, respectively. The fits are successful and based on suggested in literature S.G. *P4* and S.G. *P4/ncc* structure models. The residual difference is in green. (c), (d) Comparison between computed (red) and experimental (symbols) atomic PDFs for NbTe$_4$ obtained at 299 K and 19 K. The computed PDFs are based on the results of the Rietveld fits shown in (a) and (b). The computed and experimental PDFs are similar but disagree in many important details. The disagreement is exemplified in the insets, which show fine PDF features outlined with rectangles (broken green line). The agreement improves to an acceptable level when the models are further refined against the experimental PDF data, as shown in (e) and (f). The residual difference is in blue.

For completeness, PDF-refined parameters for both models are shown in Fig. 3 (right). As can be seen in the figure, the irregularities in the temperature evolution of the super-cell parameters revealed by PDF analysis appear stronger in comparison to those revealed by Rietveld analysis, indicating that the local crystal structure of NbTe$_4$ undergoes stronger changes with the evolving CDW order in comparison to the average structure.
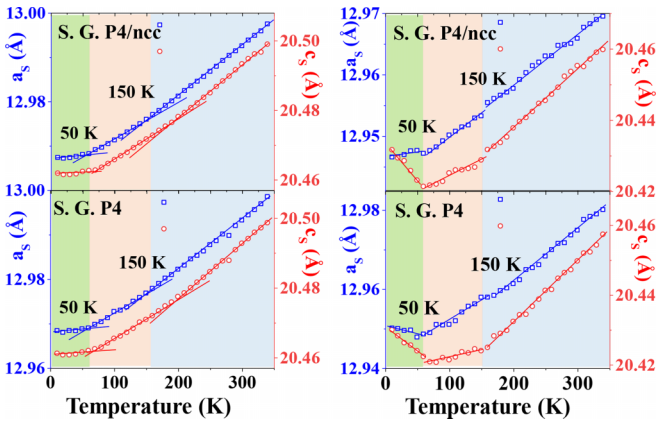

FIG. 3. Temperature evolution of tetragonal supercell parameters a_S (blue) and c_S (red) for NbTe$_4$ obtained by Rietveld (left) and PDF (right) fits. The fits are based on the S.G. *P4/ncc* and S.G. *P4* models explained in the text. The parameters show discontinuities at the temperature of IC$_1$-CDW to IC$_2$-CDW and IC$_2$-CDW to C-CDW phase transitions. The discontinuities are particularly well expressed with the PDF-refined parameters. Solid lines through the data points are used to emphasize changes in the rate of change in the lattice parameters with temperature. Areas shaded in different colors highlight temperature ranges where NbTe$_4$ exhibits IC$_1$-CDW (blue), IC$_2$-CDW (light red), and C-CDW (green) order.

B. Assessing lattice distortions in NbTe$_4$ by large-size structure modeling

As can be seen in Figs. 2(e) and 2(f), otherwise successful PDF fits constrained to $2a \times 2a \times 3c$ supercells appear unable to reproduce fine details in the experimental data, i.e., fine local structure features. To reveal the local structure of NbTe$_4$ in full detail, we carried out reverse Monte Carlo (RMC) simulations where large-size models were refined against the experimental PDF data. The initial atomic configurations featured 30720-atom, approximately 80 Å × 80 Å × 80 Å in size model boxes with an average tetragonal symmetry where Nb and Te atoms are arranged according to the rules of S.G. *P4* symmetry. Initial models based on the S.G. *P4/nnc* symmetry produced similar results. The large model boxes allowed us to explore lattice distortion patterns with a length-scale much larger than the characteristic $2a \times 2a \times 3c$ supercell of NbTe$_4$ at any temperature while maintaining the average tetragonal symmetry of the crystal lattice intact. The simulations were carried out with the help of the software FULLRMC [36]. During the simulations, no crystal symmetry related constraints were applied. Physically sensible constraints were, however, applied. In particular, atoms were not allowed to come closer to each other than the known bonding distances in NbTe$_4$. The simulations were considered complete when no further improvement of the agreement between the RMC simulated and experimental PDFs was possible to be achieved. Representative RMC fits to PDF data obtained at 299 K (IC$_1$-CDW order), 99 K (IC$_2$-CDW order), and 19 K (C-CDW order) are shown in Fig. 4. As can be seen in the figure, the RMC simulations produce structure models that fit the experimental PDFs in very fine detail. Partial Nb-Nb, Te-Te, and Te-Nb atomic PDFs computed from the models are also shown in Fig. 4. As manifested by the sharpening of the respective partial Nb-Nb PDF peaks, distances between further Nb neighbors (∼6–7.5 Å) are seen to increasingly become better defined
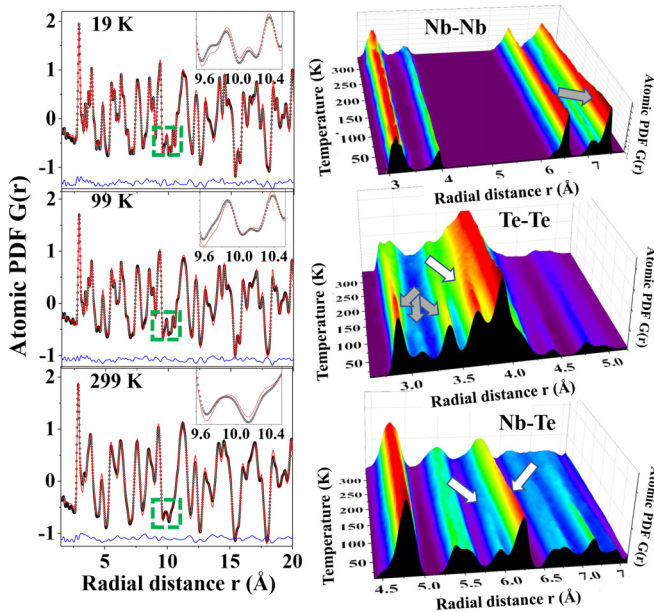
FIG. 4. Left: RMC fits (red) to experimental PDFs (black) for NbTe$_4$ obtained at 299 K, 99 K, and 19 K, where NbTe$_4$ exhibits IC$_1$-CDW, IC$_2$-CDW, and C-CDW order, respectively. The residual difference is in blue. Data in the insets illustrate the superb quality of RMC fits to fine PDF features, outlined with rectangles (dashed green line), in comparison to crystallographic PDF fits (compare with data in Fig. 2). Right: Temperature evolution of partial Nb-Nb, Te-Te, and Nb-Te atomic PDFs for NbTe$_4$, as computed from the RMC-refined models. Arrows mark changes in atomic-pair distances with evolving temperature and CDW order.

with the temperature decreasing below 150 K (see arrows), signaling the evolution of IC$_2$-CDW order into C-CDW order. The same pertains to first neighbor Te-Te distances ($\sim$2.9 Å). Here, in addition, below 200 K, a new Te-Te distance emerges at 3.8 Å. At the temperature of IC$_2$-CDW to C-CDW transition (50 K), another Te-Te distance emerges at about 3.1 Å. The evolution of Te-Nb distances appears as a combination of the evolutions of Nb-Nb and Te-Te distances, including both the emergence of new Nb-Te distances ($\sim$ 6 Å) and the sharpening of the distance's distribution with decreasing temperature (see arrows).

IV. DISCUSSION

Results from folding the 80 Å $\times$ 80 Å $\times$ 80 Å RMC derived configurations into $2a \times 2a \times 3c$ tetragonal supercells are shown in Figs. 5(a), 5(b), and S2. An analysis of the data in Figs. 5(a) and 5(b) shows that, during the evolution of IC$_1$-CDW order into IC$_2$-CDW order taking place when the temperature decreases from 299 K to 99 K, Nb-Nb distances redistribute such that distinct Nb trimers emerge [green bonding distances in Fig. 5(a)]. Concurrently, a significant shortening of Te-Te distances in the Te rectangles takes place [e.g., see the disappearance of dashed Te-Te distances in Fig. 5(b)]. The characteristic pattern of Nb separations does not seem to change significantly below 100 K but does seem to become better expressed (see the sharpening of Nb-Nb partial PDFs in Fig. 4). On the other hand, the pattern of Te distances

is seen to change significantly when the C-CDW order is approached upon cooling the sample (follow the sequence of arrows and changes in bond color/length). Overall, while the repositioning of Nb atoms along the chains (longitudinal modulation of Nb displacements) appears to drive the evolution of IC$_1$-CDW into IC$_2$-CDW order, in-plane repositioning of Te atoms (transversal modulation of Te displacements) appears to drive the evolution of IC$_2$-CDW into C-CDW order. Other structural studies have also emphasized the important role of both Nb and Te repositioning in the evolution of CDW order in NbTe$_4$ [22]. The analysis also shows (Fig. S2) that, as might be expected [16,19], the 19 K RMC configuration exhibits C-CDW order while the 99 K and 299 K RMC configurations exhibit IC-CDW order. Notably, no particular atomic displacement modes have been promoted during the RMC simulations. It is the experimental PDF data that guided the evolution of CDW order in the RMC models with temperature.

A striking feature of the electronic structure of some strongly correlated systems is the existence of symmetry protected degeneracies that impart semimetallic behavior, such as Weyl and Dirac points (DPs) [4,6,37,38]. It has been shown that non-CDW TaTe$_4$ may host DPs while, thanks to the emergence of periodic lattice distortions and related changes in the crystal symmetry, C-CDW TaTe$_4$ can host double DPs [8]. Self-consistent density functional theory (DFT) calculations including spin-orbit coupling were performed to assess the electronic structure of NbTe$_4$ using the generalized gradient approximation using the generalized gradient approximation [39] as implemented in the Vienna *ab initio* Simulation Package [40]. The energy cutoff for the plane-wave basis was set to 420 eV and k meshes of $7 \times 7 \times 7$ for the non-CDW phase and $2 \times 2 \times 2$ for the CDW phase of NbTe$_4$ were adopted. Similar to the case for non-CDW TaTe$_4$, a linear band crossing appears between the Γ-Z and M-A points in the band structure for non-CDW NbTe$_4$ (ten-atom unit cell; S.G. *P4/mcc*), leading to DPs (see Fig. S3). The band structure for C-CDW NbTe$_4$ computed from structural data obtained through PDF fits constrained to tetragonal S.G. *P4/ncc* symmetry (120-atom, $2a \times 2a \times 3c$ tetragonal supercell; Supplemental Material Table S1) is shown in Fig. 5(c). The two DPs in the band structure no longer exist. Instead, an eightfold degeneracy, equivalent to a double Dirac point (DDP), emerges at point A about 0.73 eV below the Fermi level [Fig. 5(f)]. In addition, a new fourfold degeneracy, equivalent to a DP, emerges 0.47 eV below the Fermi level at point Z [Fig. 5(e)]. The band structure of C-CDW NbTe$_4$ computed from structural data obtained through RMC fits, which break the S.G. *P4/ncc* symmetry constraints locally to fully take into account fine PDF/local structural features (120-atom, $2a \times 2a \times 3c$ tetragonal supercell; Supplemental Material Table S2) is shown in Fig. 5(d). As can be seen in the figure, because of the locally broken symmetry, the topology of the band structure is modified to such an extent that the degeneracy of band crossings at point A is partially lifted [see Fig. 5(g)] and the DDP is transformed into a DP.

Angle-resolved photoemission spectroscopy experiments on C-CDW TaTe$_4$ found evidence for band folding that is a prerequisite for the emergence of higher-order Dirac fermions but failed to reproduce the DFT predicted band structure in
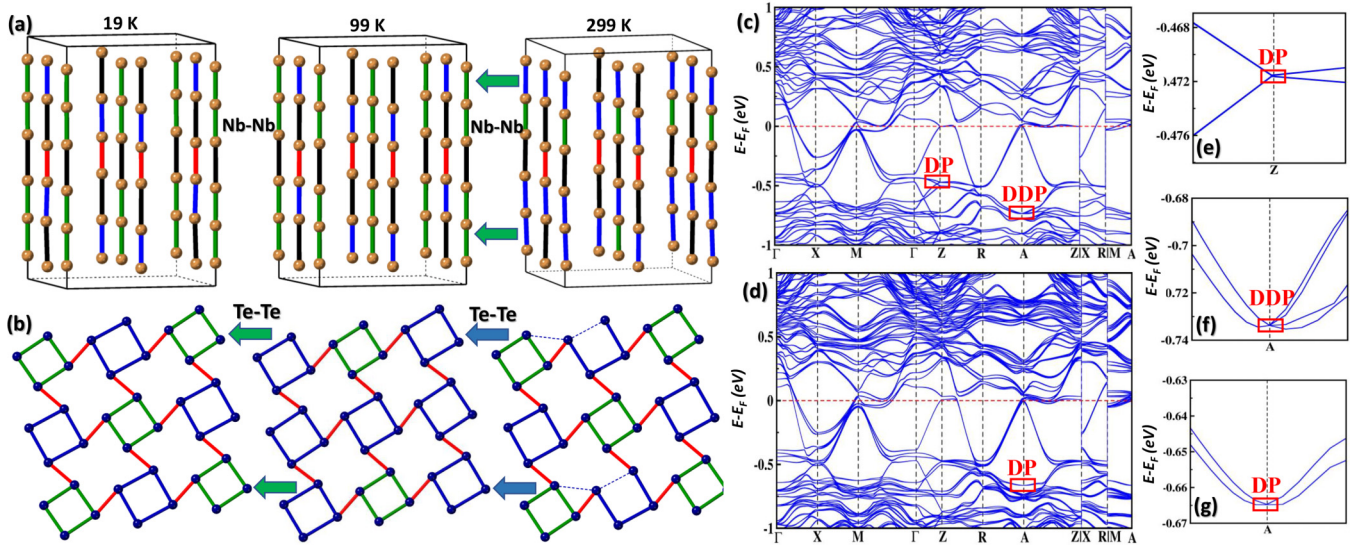
FIG. 5. (a) Characteristic distances between Nb atoms in a $2a \times 2a \times 3c$ tetragonal cell of NbTe$_4$ at 299 K, 99 K, and 19 K, where it exhibits IC$_1$-CDW, IC$_2$-CDW, and C-CDW order, respectively. Distances shorter than 3.1 Å are given in red. Distances falling in the range from 3.1 Å to 3.2 Å, from 3.2 Å to 3.35 Å, and from 3.25 Å to 4 Å are given in green, blue, and black, respectively. (b) Characteristic distances between atoms in Te planes in NbTe$_4$ at 299 K, 99 K, and 19 K. Te-Te dimerlike distances (red) bridging rectangles of Te atoms appear shorter than 3.0 Å at any given temperature. Distances between Te atoms falling in the range from 3.0 Å to 3.25 Å and from 3.25 Å to 3.5 Å are given in green and blue, respectively, while those longer than 3.5 Å are given as a dashed line. Arrows emphasize changes in the length of particular atomic-pair distances with decreasing temperature. The configurations presented in (a) and (b) are obtained by folding 30720-atom RMC models into 120-atom tetragonal unit cells. Each of the atoms in the configurations is located at the center of gravity of a distribution of 256 Nb/Te atoms, the positions of which have been individually RMC refined against experimental PDF data. The band structure for C-CDW NbTe$_4$ at 19 K as computed from 120-atom tetragonal supercell models where the atomic positions are obtained by crystallographic (S.G. *P4/ncc* symmetry strictly imposed) and RMC (locally broken S.G. *P4/ncc* symmetry) fits to atomic PDF data is shown in (c) and (d), respectively. Red rectangles outline Dirac points (DPs) and double Dirac points (DDPs). The DP and DDP in (c) are shown enlarged in (e) and (f), respectively. The DP in (d) is shown enlarged in (g).

good detail [8]. The disagreement has been attributed to strong electron-electron correlation effects, but unaccounted for local lattice distortions that coexist with the emerged $2a \times 2a \times 3c$ tetragonal superstructure may well be another major factor that contributes to it. Lattice distortions are indeed demonstrated to induce distinct topological states [7,41,42].

V. CONCLUSION

In summary, atomic PDF analysis coupled to computer modeling allows one to assess both the average crystal structure and the lattice distortions in complex CDW systems, producing the most probable positions of the constituent atoms. The positions may be constrained to a particular lattice symmetry suggested by traditional or superspace crystallographic studies, group theory, or DFT predictions. In addition, when prompted by the experimental data, the positions can deviate from it locally so that fine-structure features are fully reproduced. This technique allowed us to resolve atomic displacement modes in CDW phases of NbTe$_4$ without a priori crystal structure knowledge. It helped confirm the expected S.G. *P4/ncc*-type structure for C-CDW NbTe$_4$ and provided

a solid ground for electronic structure calculation. The calculations suggest that C-CDW NbTe$_4$ may harbor topological electronic states and, therefore, is a potential member of the emerging family of topological superconductors. Given the presence of significant local lattice distortions, however, the multiplicity of the states may be lower than anticipated based on average crystal structure studies. The results indicate that the marked flexibility of the crystal lattice in CDW systems in general, and in particular in transition metal tetratellurides, must be accounted for when their rich physics is considered.

[1] P. Monceau, Electronic crystals: An experimental overview, Adv. Phys. **61**, 325 (2012).

[2] K. Rossnagel, On the origin of charge-density waves in select layered transition-metal dichalcogenides, J. Phys.: Condens. Matter **23**, 213001 (2011).

[3] S. van Smaalen, The Peierls transition in low-dimensional electronic crystals, Acta Crystallogr., Sect. A: Found. Crystallogr. **61**, 51 (2005).

[4] B. Brandlyn, J. Cano, Zh. Wang, M. G. Vergniory, C. Felser, R. J. Cava, and B. A. Bernevig, Beyond Dirac and Weyl fermions: Unconventional quasiparticles in conventional crystals, Science **353**, 558 (2016).

[5] C. W. Chen, J. Choe, and E. Morosan, Charge density waves in strongly correlated electron systems, Rep. Prog. Phys. **79**, 084505 (2016).

[6] X. Zhang, Q. Gu, H. Sun, T. Luo, Y. Liu, Y. Chen, Z. Shao, Z. Zhang, S. Li, Y. Sun, Y. Li, X. Li, S. Xue, J. Ge, Y. Xing, R. Comin, Z. Zhu, P. Gao, B. Yan, Ji Feng, M. Pan, and J. Wang, Eightfold fermionic excitation in a charge density wave compound, Phys. Rev. B **102**, 035125. (2020).

[7] B. J. Wieder, Y. Kim, A. M. Rappe, and C. L. Kane, Double Dirac semimetals in three dimensions, Phys. Rev. Lett. **116**, 186402 (2016).

[8] Y. Zhang, R. Zhou, H. Wu, Ji S. Oh, S. Li, J. Huang, J. D. Denlinger, M. Hashimoto, D. Lu, S.-Kwan Mo, K. F. Kelly, R. J. Birgeneau, B. Lv, G. Li, and M. Yi, Charge order induced Dirac pockets in the nonsymmorphic crystal TaTe$_4$, Phys. Rev. B **108**, 155121 (2023).

[9] Y. Yuan, W. Wang, Y. Zhou, X. Chen, C. Gu, C. An, Y. Hou, B. Zhang, C. Chen, R. Zhang, and Z. Yang, Pressure-induced superconductivity in topological semimetal candidate TaTe$_4$, Adv. Electron. Mater. **6**, 1901260 (2020).

[10] X. Yang, Y. Zhou, M. Wang, H. Bai, X. Chen, C. An, Y. Zhou, Q. Chen, Y. Li, and Z. Wang, Pressure induced superconductivity bordering a charge-density-wave state in NbTe$_4$ with strong spin-orbit coupling, Sci. Rep. **8**, 6298 (2018).

[11] K. Selte, A. Kjekshus, C. S. Petersen, H. Halvarson, and L. Nilsson, On the crystal structure of NbTe$_4$, Acta Chem. Scand. **18**, 690 (1964).

[12] F. W. Boswell and A. Prodan, Structural changes in the discommensurate distortion waves of NbTe$_4$ on cooling, Phys. Rev. B **34**, 2979, (1986).

[13] F. W. Boswell, A. Prodan, and J. K. Brandon, Charge-density waves in the quasi-one-dimensional compounds NbTe$_4$ and TaTe$_4$, J. Phys. C: Solid State Phys. **16**, 1067 (1983).

[14] B. Guster, M. Pruneda, P. Ordejón, and E. Canadell, Competition between Ta-Ta and Te-Te bonding leading to the commensurate charge density wave in TaTe$_4$, Phys. Rev. B **105**, 064107, (2022).

[15] M. B. Walker and R. Morelli, NbTe$_4$: A model for a class of incommensurate-to-incommensurate phase transitions, Phys. Rev. B **38**, 4836, (1988).

[16] K. D. Bronsema, S. van Smaalen, J. L. De Boer, G. A. Wiegers, F. Jellinek, and J. Mahy, The determination of the commensurately modulated structure of tantalum tetratelluride, Acta Crystallogr., Sect. B: Struct. Sci. **43**, 305 (1987).

[17] S. van Smaalen, K. D. Bronsema, and J. Mahy, The determination of the incommensurately modulated structure of niobium tetratelluride, Acta Crystallogr., Sect. B: Struct. Sci. **42**, 43 (1986).

[18] A. Prodan and F. W. Boswell, A dualistic interpretation of the incommensurate modulated structures of NbTe$_4$, Acta Crystallogr., Sect. B: Struct. Sci. **43**, 165 (1987).

[19] A. Prodan, F. W. Boswell, J. C. Bennett, J. M. Corbett, T. Vidmar, V. Marinković, and A. Budkowski, Structures of two low-temperature incommensurate NbTe$_4$ phases, Acta Crystallogr., Sect. B: Struct. Sci. **46**, 587 (1990).

[20] R. Morelli and M. B. Walker, Novel mechanism for the incommensurate-to-incommensurate phase transition in NbTe$_4$, Phys. Rev. Lett. **62**, 1520 (1989).

[21] J. Kusz and H. Böhm, The low-temperature structure of NbTe$_4$, Acta Crystallogr., Sect. B: Struct. Sci. **50**, 649 (1994).

[22] J. A. Galvis, A. Fang, D. Jimenez-Guerrero, J. Rojas-Castillo, J. Casas, O. Herrera, A. C. Garcia-Castro, E. Bousquet, I. R. Fisher, and A. Kapitulnik, Nanoscale phase-slip domain walls in the charge density wave state of the Weyl semimetal candidate NbTe$_4$, Phys. Rev. B **107**, 045120 (2023).

[23] S. Tadaki, N. Hino, T. Sambongi, K. Nomura, and F. Lévy, Electrical properties of NbTe$_4$ and TaTe$_4$, Synth. Met. **38**, 227 (1990).

[24] P. Juhás, T. Davis, C. L. Farrow, and S. J. L. Billinge, PDFgetX3: A rapid and highly automatable program for processing powder diffraction data into total scattering pair distribution functions, J. Appl. Crystallogr. **46**, 560 (2013).

[25] See Supplemental Material at http://link.aps.org/supplemental/10.1103/PhysRevB.108.174112 for for [brief description of the material], which also contains Refs. [20,42].

[26] J. Rodriguez-Carvajal, Recent advances in magnetic structure determination by neutron powder diffraction, Phys. B (Amsterdam, Neth.) **192**, 55 (1993).

[27] H. Böhm and H.-G. von Schnering, The modulated structure of niobium tetratelluride NbTe$_4$, Z. Kristallogr. -Cryst. Mater. **171**, 41 (1985).

[28] D. J. Eaglesham, D. Bird, R. L. Withers, and J. W. Steeds, Microstructural behaviour in the CDW states of NbTe$_4$ and TaTe$_4$; domains, discommensurations and superlattice symmetry, J. Phys. C: Solid State Phys. **18**, 1 (1985).

[29] T. Egami and S. J. L. Billinge, *Underneath the Bragg Peaks*, 2nd ed. (Pergamon, Amsterdam, 2003).

[30] V. Petkov, *Characterization of Materials* (Wiley, New York, 2012).

[31] H. J. Kim, C. D. Malliakas, A. T. Tomić, S. H. Tessmer, M. G. Kanatzidis, and S. J. L. Billinge, Local atomic structure and discommensurations in the charge density wave of CeTe$_3$, Phys. Rev. Lett. **96**, 226401 (2006).

[32] V. Petkov, K. Chapagain, S. Shastri, and Y. Ren, Genesis of the periodic lattice distortions in the charge density wave state of 2*H*-TaSe$_2$, Phys. Rev. B **101**, 121114(R) (2020).

[33] V. Petkov, K. Chapagain, J. Yang, S. Shastri, and Y. Ren, Exotic bonding interactions and coexistence of chemically distinct periodic lattice distortions in the charge density wave compound TaTe$_2$, Phys. Rev. B **102**, 024111 (2020).

[34] V. Petkov, J. Yang, S. Shastri, and Y. Ren, Hierarchy among the crystal lattice, charge density wave, and superconducting orders in transition metal dichalcogenides, Phys. Rev. B **102**, 134119 (2020).

[35] V. Petkov, J. E. Peralta, B. Aoun, and Y. Ren, Atomic structure and Mott nature of the insulating charge density wave phase of 1T−TaS$_2$, J. Phys.: Condens. Matter **34**, 345401 (2022).

[36] B. Aoun, Stochastic atomic modeling and optimization with *fullrmc*, J. Appl. Crystallogr. **55**, 1664 (2022).

[37] O. Vafek and A. Vishwanath, Dirac fermions in solids: From high-T_c cuprates and graphene to topological insulators and Weyl semimetals, Ann. Rev. Condens. Matter Phys. **5**, 83 (2014).

[38] I. F. Herbut, Time reversal, fermion doubling, and the masses of lattice Dirac fermions in three dimensions, Phys. Rev. B **83**, 245445 (2011).

[39] J. P. Perdew, K. Burke, and M. Ernzerhof, Generalized gradient approximation made simple, Phys. Rev. Lett. **77**, 3865 (1996).

[40] G. Kresse and J. Furthmüller, Efficient iterative schemes for *ab initio* total-energy calculations using a plane-wave basis set, Phys. Rev. B **54**, 11169 (1996).

[41] C. Brune, C. X. Liu, E. G. Novik, E. M. Hankiewicz, H. Buhmann, Y. L. Chen, X. L. Qi, Z. X. Shen, S. C. Zhang, and L. W. Molenkamp, Quantum Hall effect from the toplogical surface states of strained bulk HgTe, Phys. Rev. Lett. **106**, 126803 (2011).

[42] M. Dusek, V. Petricek, M. Wunschel, R. E. Dinnenbier, and S. van Smaalen, Refinement of modulated structures against X-ray powder diffraction data with *JANA*2000, J. Appl. Crystallogr. **34**, 398 (2001).